Acta Materialia 210 (2021) 116830

Contents lists available at ScienceDirect

Acta Materialia

journal homepage: www.elsevier.com/locate/actamat

Full length article

Anisotropic strengthening of nanotwin bundles in heterogeneous nanostructured Cu: Effect of deformation compatibility

H.Z. Zhao[a,b], Z.S. You[c], N.R. Tao[a], L. Lu[a,1,*]

[a] Shenyang National Laboratory for Materials Science, Institute of Metal Research, Chinese Academy of Sciences, Shenyang 110016, China
[b] School of Materials Science and Engineering, University of Science and Technology of China, Shenyang 110016, China
[c] Herbert Gleiter Institute of Nanoscience, Nanjing University of Science and Technology, Nanjing 210094, China

ARTICLE INFO

Article history:
Received 24 November 2020
Revised 1 March 2021
Accepted 20 March 2021
Available online 25 March 2021

Keywords:
Heterogeneous nanostructure
Anisotropic deformation
Nanotwins
Strain partitioning
Deformation compatibility

ABSTRACT

Anisotropic tensile behaviors of a heterogeneous nanostructured Cu composed of isotropic nanograin matrix and anisotropic nanotwin bundles were investigated under loading directions parallel, normal, and 45° inclined to the twin boundaries (TBs). Distinct from the anisotropic strengthening effect in the homogeneous nanotwinned (NT) counterpart, the heterostructure exhibits the highest strength under parallel tension, and moderate strength under normal tension. High-resolution digital image correlation analysis indicated an orientation-dependent deformation compatibility between the nanotwin bundles and nanograin matrix, i.e., compatible deformation in the parallel orientation; but significant incompatibility in orientations both normal and 45° inclined to TBs. The results reveal that the strengthening effect of nanotwins in heterogeneous nanostructure is not only dependent on the strength of themselves, but also influenced by the deformation compatibility with surrounding components. The orientation-dependent deformation compatibility was attributed to the interactions between isotropic shear bands in nanograin matrix and anisotropic deformation in nanotwin bundles.

1. Introduction

Heterogeneous structures (HS), including nanotwinned structure [1,2], dual-phase structure [3,4], heterogeneous lamellar structure [5,6], gradient structure [7,8], and harmonic structure [9], etc., which are constructed by components with dramatic differences in microstructure, length scale or chemical composition, have attracted extensive interest in the past few years due to their superior mechanical properties. The combination of high strength, considerable ductility [10], enhanced strain hardening capacity [7], and improved fatigue and fracture resistances [11,12] can be achieved in such heterogeneous metallic materials, which are generally not attainable in conventional homogeneous materials. Generally, the improved integrated mechanical properties in heterogeneous materials are supposed to be arising from heterogeneous deformation induced strengthening or strain hardening [13] intimately related to mutual constraint of microstructural components with strong mechanical discrepancy.

When high density of multiple nanotwins, namely nanotwin bundles (NTBs), are embedded into a nanograin (NG) matrix, a high strength is achievable with considerable fracture toughness maintained [14–18], where NTBs act as ideal strengthening and toughening components to the NG matrix. In principle, TBs are effective in blocking dislocation motion; at the same time, they retain ample room for dislocation accumulation and storage, and resist micro-void nucleation and fracture [2,19–21]. For instance, the 316L austenite stainless steels can be strengthened to as high as ~1.3 GPa by embedding a volume fraction of ~24% NTBs through dynamic plastic deformation (DPD). The strength of NTBs is estimated to be ~2.0 GPa [14]. Similar strengthening effect was also achieved in heterogeneous nanostructured Cu [22–24], Cu–Zn alloy [25,26], Cu–Al alloy [27] and other metallic materials composed of NTBs and nano-grains or coarse-grains as matrix [28–30].

In spite of exciting success in strengthening various metals and alloys by introducing NTBs, studies regarding the influence of TB orientation on their strengthening effect are still missing, owing to the limited available sample dimensions [31]. It is well-known that the heterogeneity of length scale in the nanotwins unit (with large twin length in the micrometer scale while tiny twin thickness in the nanometer scale) leads to three different dislocation modes in the plastic deformation: (i) dislocation pile-up and slip transfer across TBs (Hard Mode I), (ii) threading dislocation glide in the

* Corresponding author.
E-mail address: llu@imr.ac.cn (L. Lu).

[1] Lei Lu was an Editor of the journal during the review period of the article. To avoid a conflict of interest, Lei Lu was blinded to the record and another editor processed this manuscript.

https://doi.org/10.1016/j.actamat.2021.116830
1359-6454/

twin/matrix lamellar channels (Hard Mode II), and (iii) TB migration mediated by motion of partial dislocations parallel to TBs (Soft Mode, also named Mode III) [32,33]. These three dislocation modes dominate the plastic deformation with normal, parallel and 45° inclined to TBs, respectively, resulting in strong anisotropy in both yield strength and strain hardening [32]. As a result, the electrodeposited Cu with homogeneous highly oriented nanoscale twins exhibits highest strength when the loading axis is normal to TBs, moderated strength parallel to TBs, and lowest strength inclined 45° to TBs [32].

Besides anisotropic strengthening, the orientation-dependent deformation compatibility should also be taken into account since the different strain partitioning is unavoidably prevalent due to the distinctly diverse deformation behavior of NTBs at different loading directions [5,13,34–36]. The deformation compatibility would also influence the global mechanical behavior of the materials with heterogeneous structures [5,6,37,38]. Previous studies [39,40] in the nanotwinned austenitic steel have shown that the nanotwinned grains deform compatibly with the surrounding recrystallized grains without causing noticeable strain localization at their interfaces [41,42]. However, only the case with loading direction almost parallel to the TBs is studied, both the anisotropic strengthening and deformation compatibility related to NTBs in the hybrid microstructure are still elusive.

In this study, we investigate the anisotropic tensile behavior of the heterogeneous nanostructured Cu composed of NTBs and NG matrix. This is a bulk sample with sufficiently large size in three dimensions; as a consequence, tensile tests can be conducted with loading directions parallel to, normal to and inclined 45° with respect to TBs. Evolution of local strain and strain partitioning in the heterogeneous microstructure are studied by interrupted tensile tests in combination with high-resolution digital image correlation (HR-DIC) analysis.

2. Experimental details

2.1. Sample preparation

High-purity coarse-grained Cu (99.995 wt.%) with an average grain size of ~360 μm was processed on a DPD facility at liquid nitrogen temperature. The set-up and processing procedures have been described in detail in Refs. [43,44]. In this study, to synthesize bulk DPD Cu samples sufficiently thick for tensile tests in different directions, cylindrical Cu samples with an initial height of 62 mm and a diameter of 30 mm were prepared and subjected to multiple DPD impactions. Limited by the impact energy of the DPD facility, the treatment process was interrupted when the sample height was reduced to ~38 mm. A cylindrical sample with a diameter of 30 mm was then cut from the center of the intermediate product by electrical discharge machining (EDM), and subjected to the DPD treatment again. The final dimension of the DPD Cu disc was ~14 mm in thickness and ~45 mm in diameter, with a total accumulative strain of ~1.5. The accumulative strain here is defined as $\varepsilon = \ln(h_i/h_f)$, where the h_i and h_f are the initial and final sample thicknesses, respectively.

2.2. Mechanical tests

Uniaxial tensile tests were performed on an Instron 5848 micro-tester at a strain rate of 5×10^{-3} s^{-1} at ambient temperature. A contactless MTS LX300 laser extensometer with a displacement resolution of 1 μm is used to accurately measure the imposed strain. Dog-bone-shaped tensile specimens were cut from the DPD disc by EDM with a length of 5 mm, a width of 2 mm, and a thickness of 0.5 mm in the gauge section. To probe the orientation dependence of the mechanical response of the DPD Cu, we conducted tensile tests in three different orientations, i.e., parallel, normal, and 45° inclined to TBs (hereafter referred to as sample-P, sample-N and sample-I, respectively), as schematically shown in Fig. 1a. The stress-strain curves of each sample were obtained from at least three individual tensile tests to confirm the reproducibility and to get the standard errors. The yield strengths were calculated at 0.2% offset strain.

Nanoindentation tests were performed on the cross-section of DPD Cu with the indenter pressed parallel to the TBs, using an Agilent G200 Nanoindenter with a load of 5 mN and a loading time of 10 s. Before the indentation tests, a region containing both nanotwins and nanograins were identified by an FEI Nova NanoSEM 460 scanning electron microscopy (SEM) under backscattered electron (BSE) imaging mode. Then a regular array of indentations covering the identified regions were tested to investigate the hardness and elastic modulus of the different microstructural components. The spacing of two adjacent indentations was ~10 μm to avoid any overlapping effect.

2.3. Interrupted tensile experiments and digital image correlation

The interrupted tensile tests were performed by using the Instron 5848 micro-tester while the ex-situ observations of the tensile specimens were conducted by using an FEI Nova NanoSEM 450 SEM under secondary electron imaging mode. The initial reference images with typical regions that containing both NTBs and NG matrix were taken prior to tensile tests from the gauge that were previously etched by a Fe(III) chloride + HCl solution to visualize the microstructure and produce random speckle patterns for DIC measurements. After tensile deformation at three given strains of 1.0% (near the maximum stress point), 1.5% (after the maximum stress point) and 2.0%, the corresponding SEM images in the tensile-deformed samples were acquired from the regions same with the initial reference images, respectively.

The in-plane strain fields at the microscopic scale were obtained using an open-source DIC Matlab program (Ncorr), which is constructed by comparing the SEM images at each deformation step with the corresponding initial reference images. Further, a post-processing application (Ncorr post CSTool) was also implemented to extract and display the strains along a certain profile.

2.4. Microstructure and fracture feature characterizations

The microstructures of as-processed and tensile-deformed DPD Cu were characterized by the FEI Nova NanoSEM 460 SEM with BSE imaging mode, while the more detailed microstructure of as-processed DPD Cu was examined by a JEOL 2010 transmission electron microscopy (TEM) operated at an accelerating voltage of 200 kV. SEM samples were first mechanically polished and then electro-polished in an electrolyte of phosphoric acid (25 Vol.%), alcohol (25 Vol.%) and deionized water (50 Vol.%) under 5 V for 30 s at ambient temperature. The TEM foils with a diameter of ~3 mm were thinned by twin-jet polishing in the same electrolyte at a temperature of −10°C. The microstructure evolution of the etched specimens and the fracture surfaces after tensile tests were examined by the FEI Nova NanoSEM 450 SEM under secondary electron imaging mode.

3. Results

3.1. Microstructure

The SEM images in Fig. 1b show the three-dimensional (3D) microstructure of DPD Cu along the radial direction (RD), tangential direction (TD) and axial direction (AD). Observations on transverse

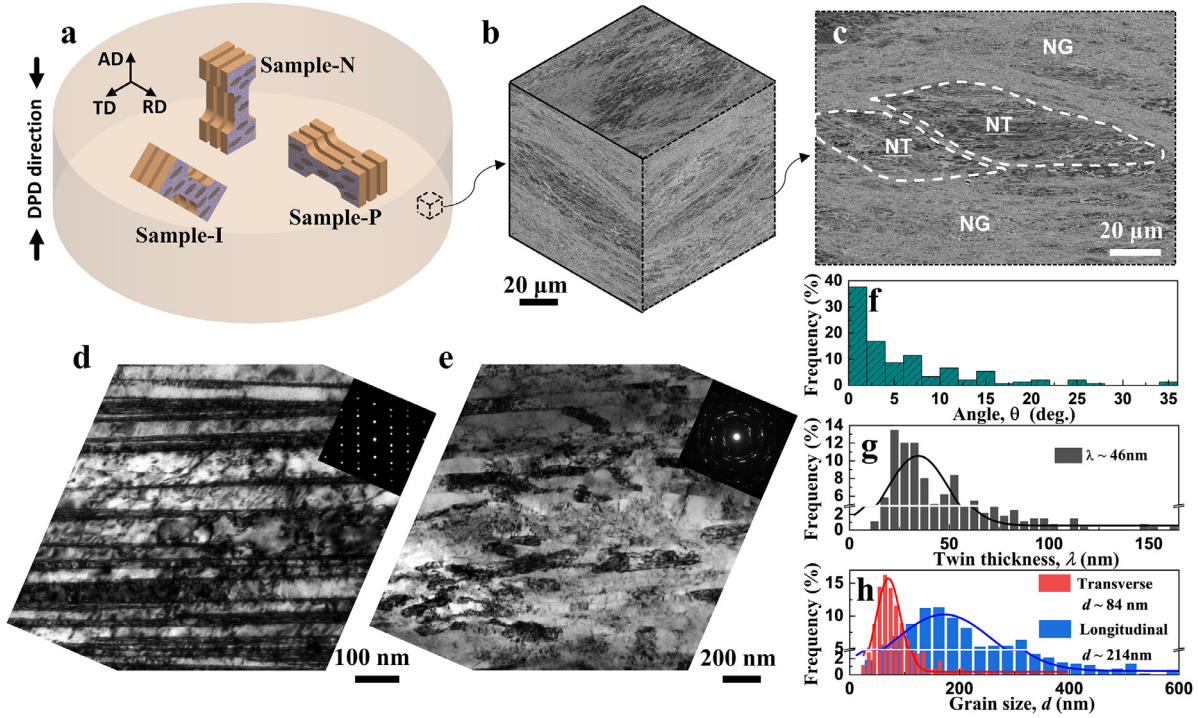

Fig. 1. (a) Schematic of the tensile specimens and their orientations in the DPD disc. (b) SEM images projected on a cube to visualize the microstructure of DPD disc in the radial direction (RD), tangential direction (TD) and axial direction (AD), respectively. (c) Typical cross-sectional microstructure of DPD Cu, showing nanotwins (denoted as NT, the underscore indicated the direction parallel to TBs, the same as that in following figures) in the form of bundles embedded in a matrix of nanograins (denoted as NG). (d) Detailed TEM observation showing NTs with a high density of dislocations accumulated at the TBs and the corresponding SAED pattern. (e) Bright-field of the elongated nanograins and the SAED pattern of the corresponding area. (f) Statistical angle distribution of TB traces with respect to the horizontal direction. (g) Twin lamellae thickness distribution and (h) transverse and longitudinal nanograins size distribution.

plane (Fig. 1c) clearly reveal a hybrid microstructure with spindle-shaped NTBs (outlined by dash lines) embedded in NG matrix. The NTBs with an average longitudinal size of 86 ± 18 μm and an average transverse size of 29 ± 9 μm occupy a volume fraction of ~30%. Fig. 1f shows the statistical histogram of the inclination angles of TBs within the NTBs with respect to the compression plane (horizontal direction in Fig. 1c). Evidently, over 80% of the TBs are inclined smaller than 10° to the horizontal direction, namely they are predominately perpendicular to the DPD compression direction (marked by the double arrows in Fig. 1a). TEM observations in Fig. 1d show that plenty of dislocations are present at TBs and inside twin interiors. The average thickness of twin/matrix lamellae is ~46 nm (Fig. 1g). Except for the nanotwin bundles, the remainder is nanograins, as revealed by TEM observations in Fig. 1e. Most nanograins are aligned and slightly elongated with an aspect ratio of ~2.5. The average transverse and longitude grain sizes are ~84 nm and ~214 nm, respectively (Fig. 1h). The selected area electron diffraction (SAED) pattern in Fig. 1e indicates that the randomly oriented nanograins are separated by high-angle grain boundaries.

3.2. Mechanical properties

Fig. 2a displays the engineering stress-strain curves for the DPD Cu specimens under different loading orientations. Compared with their coarse-grained counterpart, all the DPD Cu samples show high strength but limited uniform ductility, as generally observed in the severely deformed metals [45]. Meanwhile, the mechanical response of DPD Cu is significantly orientation dependent. Sample-P exhibits the highest strength, with yield strength σ_{ys} of 535 ± 4 MPa and ultimate tensile strength σ_{uts} of 580 ± 5 MPa; whereas sample-N displays lower strengths (σ_{ys} = 427 ± 2 MPa and σ_{uts} = 483 ± 9 MPa) and lower fracture elongation (ε_f ~ 3.4%) in comparison to that of sample-P (ε_f ~ 4.5%). Sample-I with the loading direction inclined 45° to TBs shows the lowest strength (σ_{ys} = 367 ± 3 MPa and σ_{uts} = 468 ± 6 MPa) but the flow stress decreases slowly after a small yield peak, meaning a higher resistance to localized deformation.

Statistical data in Fig. 2b indicated that the average nanoindentation hardness in NT regions is 2.58 ± 0.13 GPa, which is ~10% higher than the value in NG regions (2.31 ± 0.24 GPa). While the elastic modulus is quite close between the two components with the average value of 156.6 ± 7.5 GPa in NT regions and 155.4 ± 9.6 GPa in NG regions (Fig. 2c), implying that the NTBs would elastically homogeneous with the NG matrix during the tensile deformation.

3.3. Local strain measurement

In order to explore the deformation behavior of the samples at the micro level, we quantified the local plastic strain distributions by using interrupted tensile tests in combination with HR-DIC full-field strain analysis. The local strain distributions of the samples at applied strains of 1.0%, 1.5% and 2.0% are shown in Figs. 3(a1-a3), (b1-b3) and (c1-c3), respectively, where the strain maps with 50% transparency are overlapped with the corresponding SEM images and the boundaries of NTBs are outlined by black dash lines. Obviously, the plastic deformation is rather heterogeneous at the microscale. In particular, the deformation in sample-P (Figs. 3(a1-a3)) is concentrated in several bands across both NT and NG regions, without any strain partitioning detected between the two regions. The strain-localized bands are oriented at ~45° to tension axis in NG regions while roughly perpendicular to tension axis in NT region. The extracted profiles (vertical dash lines in Figs. 3(a1-a3)) show that the cross-section strain distributions increase with increasing applied strain (Fig. 3(a4)). It is noteworthy that the peaks of strain gradient curves (indicated by the black ar-

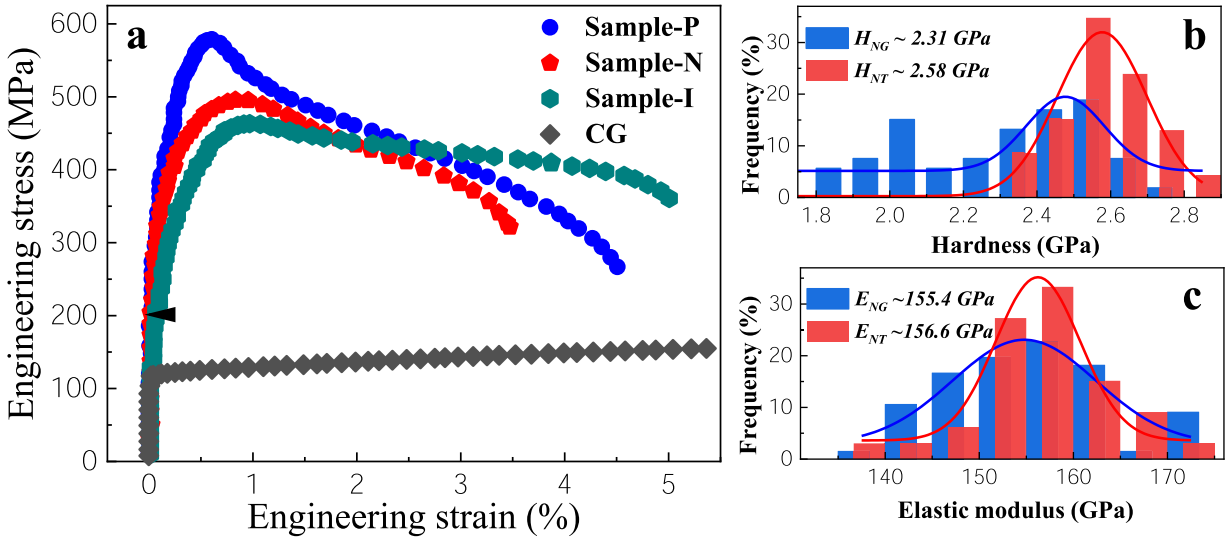

Fig. 2. (a) Tensile engineering stress-strain curves for the differently oriented specimens and the coarse-grained (CG) Cu counterpart for comparison. Statistical distribution of nanoindentation hardness (b) and elastic modulus (c) in the NT and NG regions.

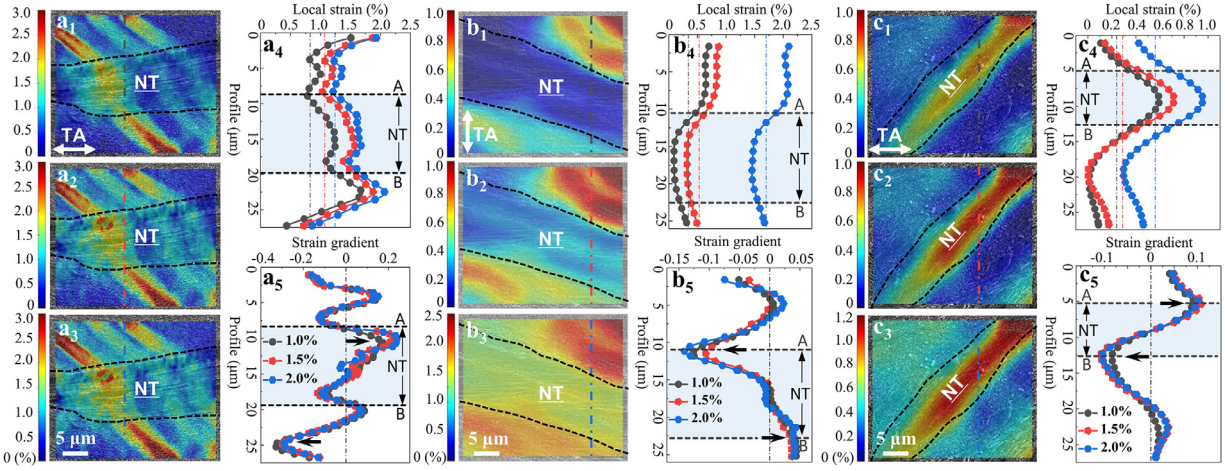

Fig. 3. Local strain fields in sample-P (a1-a3), sample-N (b1-b3) and sample-I (c1-c3) at applied strain of 1.0%, 1.5% and 2.0%, respectively. Extracted cross-section strain distributions (a4-c4) and the derived strain gradients (a5-c5) along the profiles (vertical dot-dash lines) depicted in corresponding strain maps, where the dot-dash lines in (a4-c4) are the average strain levels in each deformation stage, while the dash lines A, B indicate the position of the NT/NG interface and the black arrows in (a5-c5) indicate maximum strain gradient peaks along the profiles. The tensile axes (TA) are represented by the double-headed arrows, the same as that in the following figures.

rows in Fig. 3(a5)) do not exist at the NT/NG interfaces, suggesting that the deformations are coherent within the duplex microstructure.

The strain distribution maps for sample-N in Figs. 3(b1-b3) reveal that the plastic strain is concentrated in NG matrix while the NTBs undergo comparatively less deformation. On the contrary, the strain level of NTBs in the sample-I is much higher than that in the surrounding NG matrix (Figs.3 (c1-c3)). For comparison, the vertical cross-section strain distributions and corresponding strain gradients for sample-N and sample-I are also shown in the Figs. 3(b4, b5) and (c4, c5), respectively. Obvious strain gradients exist near the NT/NG interfaces with the derived strain gradient curves maximized along the interfaces for the both samples, meaning a significant plastic deformation incompatibility between the NTBs and NG matrix in these two samples.

3.4. Microstructure evolution

To get insight of the underlying mechanism of different strain partitioning behaviors, we investigated the microstructural evolutions with increasing applied strain by SEM observations near the necked portion of the three samples. As shown in Figs. 4(a1, b1) for sample-P, plenty of shear bands (indicated by the white arrows) making an angle of ~45° with respect to tensile axis are already initiated in NG region at the applied strain of 1.0%. Both the density and intensity of the shear bands are monotonically enhanced with increasing the applied strain up to 2.0% (Figs. 4(a2-a3, b2-b3)). Accompanying the shear bands in the NG regions, distinct line-like deformation bands (indicated by the white triangles) are also prevalent inside the NTB interiors. They are dominantly perpendicular to and spread across multiple TBs. More importantly, most of the deformation bands inside the NTBs appear to connect with the shear bands in NG region, suggesting that they are probably initiated by the impingement of shear bands in the NG matrix. These line-like deformation bands are distinguished as the traces of dislocation slip bands, which will be discussed in section 4.2 in detail.

In sample-N, a large number of shear bands (indicated by the white arrows) can be detected in NG region. Both the density and intensity of shear bands increase with the applied strains as well,

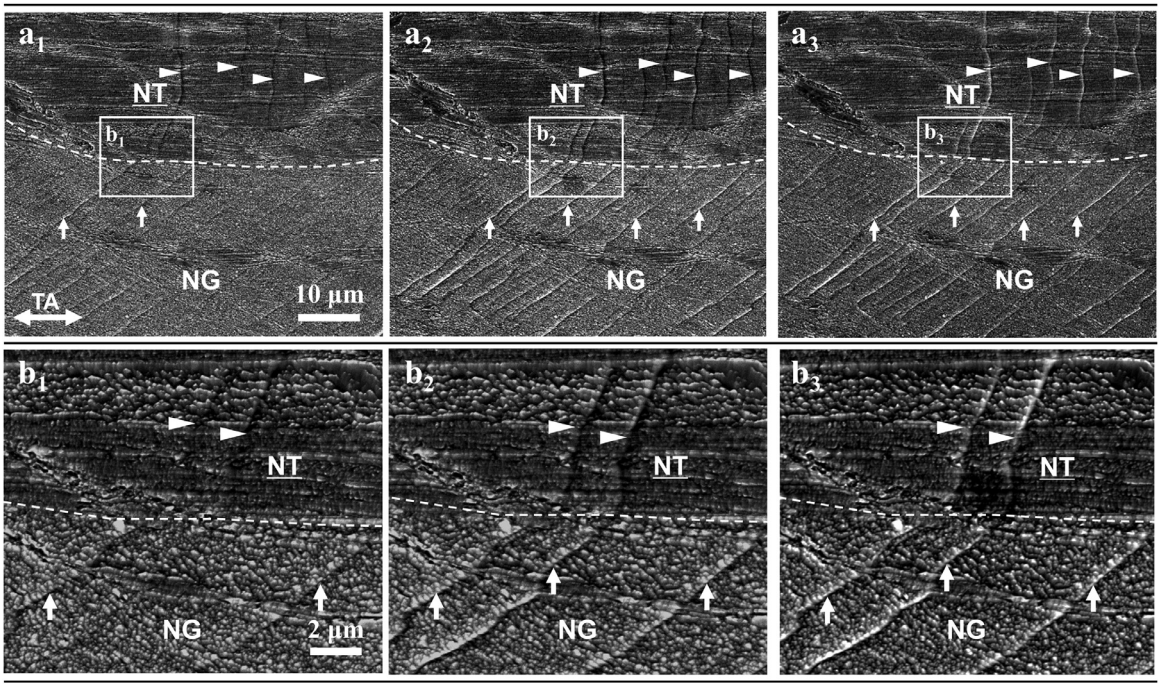

Fig. 4. SEM images of etched sample-P at the applied strain of 1.0% (a1, b1), 1.5% (a2, b2) and 2.0% (a3, b3). The nanotwinned regions are denoted as NT, while the nanograined regions are denoted as NG and the NT/NG interfaces are marked by dash lines, the same as that in Fig. 5 and 6. The interactions of micro shear bands and NTBs are highlighted in (b1-b3), corresponding to the denoted rectangle regions in (a1-a3). The arrows indicate the micro shear bands in NG region, while the triangles indicate the slip bands in NT region.

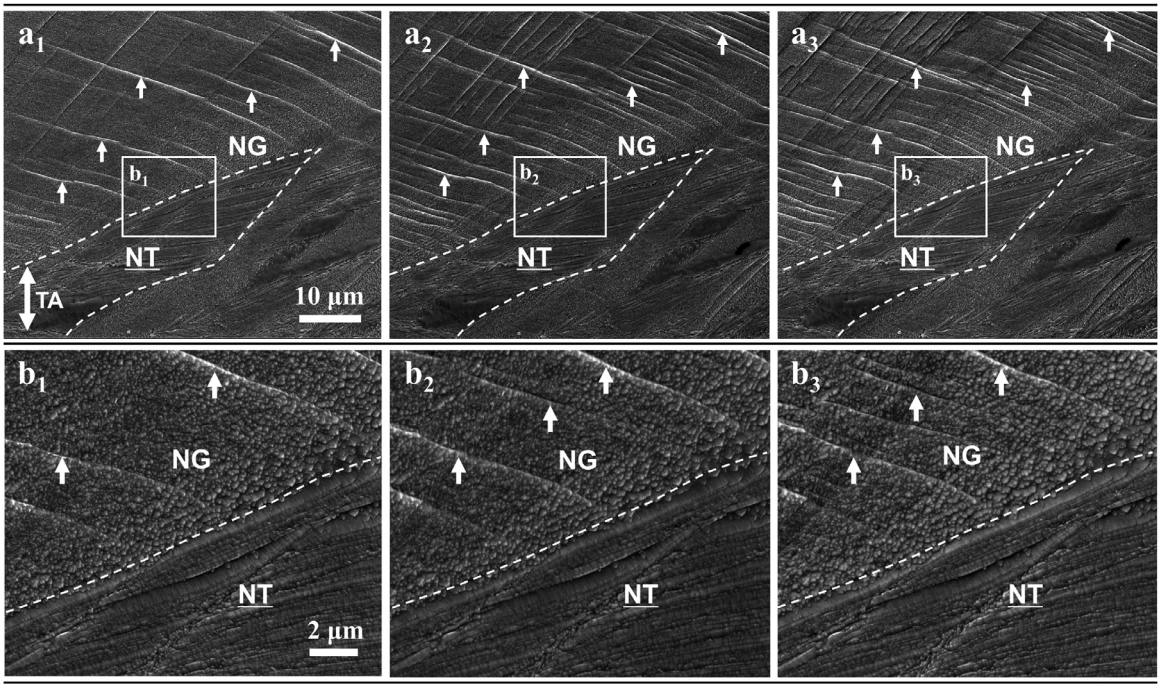

Fig. 5. SEM images of etched sample-N at the applied strain of 1.0% (a1, b1), 1.5% (a2, b2) and 2.0% (a3, b3). The interactions of micro shear bands (as indicated by white arrows) and NTBs are highlighted in (b1-b3), corresponding to the denoted rectangle regions in (a1-a3).

as shown in Fig. 5. However, distinct from the deformation process in sample-P, the shear bands do not trigger any visible deformation in the adjoining nanotwins, which means the localized deformation within the shear bands are completely impeded by the confronted NTBs. This observation is consistent with the strain field analysis in Fig. 3b, which reveals much smaller strains in the NT regions. In addition, caused by such strong obstruction of NTBs, the density of shear bands in sample-N (Fig. 5) is much higher than that in sample-P (Fig. 4) at the same applied strains, implying a much larger strain concentration in the NG matrix of sample-N.

In sample-I (Fig. 6), the shear bands evolve into different patterns along two directions of maximum resolved shear stress (±45° to tension axis). For the micro shear bands in NG region of shear

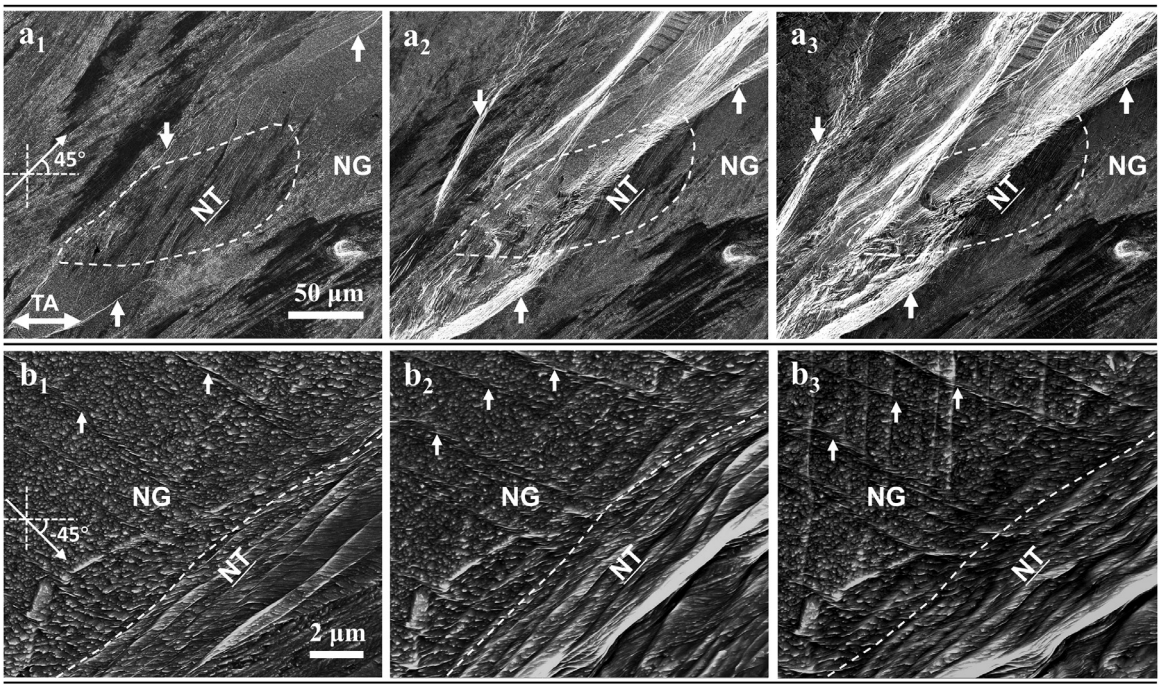

Fig. 6. SEM images of etched sample-I at applied strain of 1.0% (a1, b1), 1.5% (a2, b2) and 2.0% (a3, b3). Lower-magnification images (a1-a3) showing the interaction of micro/macro shear bands and NTBs in the direction parallel to TBs. The higher-magnification images (b1-b3) showing interactions of micro shear bands and NTB in the direction perpendicular to TBs. The arrows indicate the macro and micro shear bands.

direction parallel to TBs, indicated by white arrows in Fig. 6(a1) are first arrested by NTBs at the lower applied strain of 1.0%, and then gradually evolve into macro shear bands, which are intensive enough to cut through the NTBs, as indicated in Figs. 6(a2, a3)). While for another shear direction perpendicular to TBs, the shear bands are completely suppressed by the NTBs. As shown in Figs. 6(b1-b3), the shear bands are much weaker than the former case, suggesting that they are not responsible for the final specimen fracture.

3.5. Tensile fracture features

Observations of the fracture surfaces for the samples under different loading directions are shown in Fig. 7. Sample-P and sample-I exhibit similar shear failure along fracture planes inclined ~55° and ~50° with respect to the tensile axis, respectively, as shown in Figs. 7 (a1) and (c1); whereas in sample-N, the fracture plane is approximately perpendicular to the tensile axis.

Figs. 7(a2-c2) show the macro fracture surfaces of the three samples. The dotted lines indicate the outline of the fracture surface. Obvious localized necking occurs prior to the eventual fracture for all the samples. The reduction in area Ψ is used for evaluating the degree of strain localization:

$$\Psi = \left(A_0 - A_f\right)/A_0 \tag{1}$$

where the A_0 and A_f are the initial and necked gauge cross-sectional area, respectively. As displayed, the necking in sample-N is most serious with Ψ as high as 60%, while the sample-I has the lowest Ψ of 44%, indicating a less localized deformation. All specimens exhibit a ductile fracture surface characterized by abundant dimples (Fig. 7 (a3-c3)), which are approximately equiaxed but with somewhat different depths. The dimples are slightly deeper in sample-P, but flatter in sample-N, and become mixed with both deep and flat ones in the sample-I.

4. Discussion

4.1. Effect of deformation compatibility on global mechanical behaviors

It has been recognized that homogeneous two-dimensional (2D) nanoscale twins exhibit anisotropic strengthening under different loading directions with respect to TBs [32,33], namely significant strengthening in normal orientation, moderate strengthening in parallel orientation, and minor strengthening in 45° inclined orientation [32]. However, distinct from the anisotropic strengthening of homogeneous NT counterpart, the heterogeneous Cu with hybrid microstructure of NTBs and NG matrix exhibits highest strength when the loading direction is parallel to TBs (sample-P), as shown in Fig. 2a, and a moderate strength if the loading direction is normal to TBs (sample-N). The strain field analysis and SEM observations clearly indicate that the flow strengths of the heterogeneous nanostructured Cu not solely depend on the anisotropic strengthening of NTBs, but also closely related to orientation-dependent deformation compatibility between NTBs and NG matrix.

To quantitatively clarify the degree of deformation compatibility between NTBs and NG matrix under different loading directions, we define a parameter R as the strain ratio of two components [45], that is:

$$R = \varepsilon_{NT}/\varepsilon_{NG} \tag{2}$$

where ε_{NT} and ε_{NG} refer to the average plastic strains in NT and NG regions, respectively. The variations in average strains in the two regions and the strain ratio as a function of applied strain for the three samples are shown in Fig. 8, where the average strains are statistically analyzed from the DIC strain-field maps in Fig. 3, while the local total strain at each deformation stage is measured by attaching a “virtual extensometer” on the corresponding DIC map. Here, the deviation of the local total strains of the observation areas from the applied strains arises from the heterogeneity

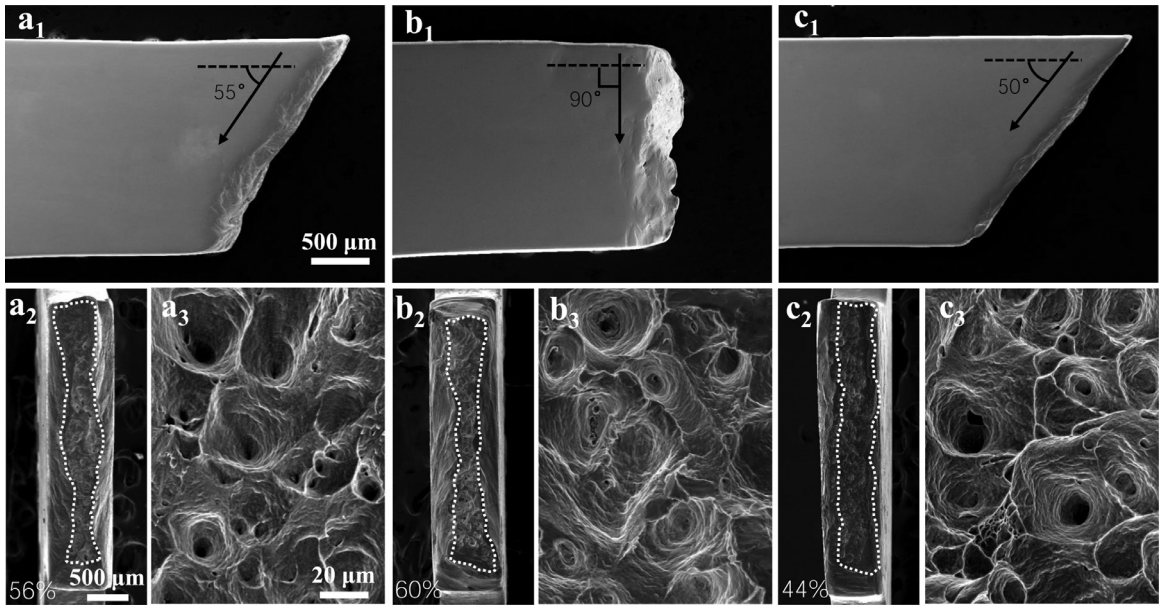

Fig. 7. Planes of the fractured tensile samples and corresponding macro/micro fracture surfaces observations for sample-P (a1-a3), sample-N (b1-b3) and sample-I (c1-c3). The angles of fracture plane with respect to the tensile axis for three samples are marked in (a1, b1, c1). The dotted lines in (a2, b2, c2) indicate the outline of the necked fracture surface, where the reduction of area is also indicated.

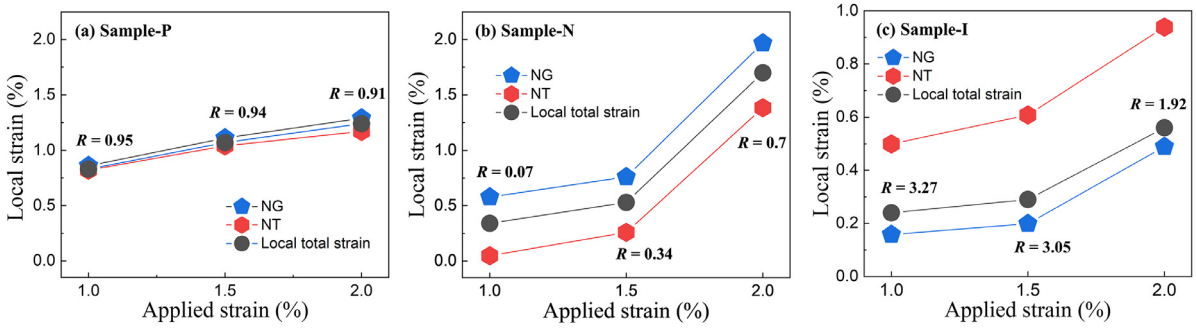

Fig. 8. Local total strains and statistical average strains in the NG and NT regions versus applied macro strains for sample-P (a), sample-N (b) and sample-I (c).

in plastic deformation throughout the whole gauge length in the tensile specimens.

As seen in Fig. 8a, the average strains in NT and NG regions in sample-P are comparable, and the strain ratio R at the applied strain of 1.0% (near the strain of necking initiation) is 0.95, in close proximity to the perfect equal-strain state of $R = 1$ [46]. This suggests that ideal co-plastic deformation is activated between NTBs and NG matrix. The plastic strain in the NTBs has already approached approximately 0.82% before necking (corresponding to the 1.0% applied strain). Considering the fact that NTBs serve as strengthening components in sample-P (evidenced by the nanoindentation result in section 3.2), we believe that the compatible co-deformation of NTBs with the NG matrix takes full advantage of their strengthening effect and effectively improves the overall flow strength.

In contrast, for sample-N, the average strain in the NG region at the 1.0% applied strain is ~0.56%, while the NTBs are nearly non-deformable with an average strain of only ~0.04% (Table 1). The strain ratio R is as low as 0.07, an indication of pronounced plastic incompatibility between the two components. Such, even though the strength of individual NTBs under normal loading direction is the highest, the strengthening effect of them is not fully functional since the NTBs do not deform plastically and cannot achieve full flow strength before necking. Consequently, the overall strength of sample-N mainly depends on that of the NG matrix. This accounts for the lower strength in sample-N, compared to that in sample-P.

There is also obvious deformation incompatibility between NTBs and NG matrix in sample-I, as shown in Fig. 8c. The plastic strain is highly localized within the NTBs, exceeding three times the average strain in NG matrix at the applied strains of 1.0 – 1.5% and nearly two times of that at the strain of 2.0%. Since the Soft Mode in nanotwins are easily activated under the inclined loading [32], the NTBs in sample-I yield and plastically deform earlier than the NG matrix. This is in correspondence with the obvious deviation from the elastic stage at a rather low stress of approximately 200 MPa in the engineering stress-strain curve of the sample-I (indicated by the black triangle in Fig. 2a). The much lower strength in NTBs accounts for the least strength in sample-I.

Another interesting finding is the different tensile fracture behaviors, as revealed in Fig. 7. Obvious shear fracture takes place in sample-P and -I (Fig. 7(a1, c1)), caused by the macro shear bands spread along the direction of maximum shear stress, whereas normal fracture, approximately perpendicular to tensile axis happens in sample-N (Fig. 7(b1)), this may be attributed to the macro shear bands are completely blocked by NTBs and cannot spread freely in the direction of maximum shear stress, as verified by the incoherent deformation between NTBs and NG matrix (Fig. 3b and 5). The NG matrix accommodates the applied strains by multiplying shear bands quantity towards transverse direction of the spec-

Table 1
Average plastic strains in NG and NT regions, strain ratio of two components and the local total strains at each deformation stage for the differently oriented specimens.

ε_{app} (%)	Sample-P				Sample-N				Sample-I				
	ε_{tot} (%)	ε_{NG} (%)	ε_{NT} (%)	R	ε_{tot} (%)	ε_{NG} (%)	ε_{NT} (%)	R	ε_{tot} (%)	ε_{NG} (%)	ε_{NT} (%)	R	$1/R$
1.0	0.83	0.86	0.82	0.95	0.35	0.56	0.04	0.07	0.24	0.15	0.49	3.27	0.31
1.5	1.07	1.11	1.04	0.94	0.53	0.76	0.26	0.34	0.29	0.2	0.61	3.05	0.33
2.0	1.24	1.29	1.17	0.91	1.72	1.97	1.38	0.7	0.56	0.49	0.94	1.92	0.52

ε_{app}, applied strain; ε_{tot}, local total strain; ε_{NG}, average plastic strain in *NG* regions; ε_{NT}, average plastic strain in *NT* regions; R, strain ratio of NT to NG.

imen or extend shear deformation towards the thickness direction. Consequently, severe lateral contraction in the necked region of sample-N with the measured Ψ as high as 60%, meaning the plastic deformation becomes very localized, results in the catastrophic failure occur earlier in sample-N, coincident with its extremely low elongation to failure of ~3.4% (Fig. 2a).

Whereas the sample-I shows higher resistance to localized deformation (Fig. 2a), this can be attributed to the activation of Soft Mode gives rise to the plasticity in NTBs, which helpful to relieve the stress intensity ahead a growing shear band and to stabilize shear bands [47]. As a result, the propagation process of macro shear bands is effectively delayed. Besides, the dispersed islands of soft NTBs promote the deformation extend widely along the gauge length and thus the sample-I shows relatively homogeneous thinning (not only confined within the necking region), as evidenced by the lowest Ψ of 44% (Fig. 7(c2)).

The different dimple depths in the three samples may be attributed to anisotropic fracture behavior in NG matrix as a result of its elongated grain shape [48–51] and to the complex interactions between the developed crack with the NTBs, which is beyond the scope of this paper and will be discussed in detail in a forthcoming paper.

4.2. Mechanisms of the orientation-dependent deformation compatibility

Due to the suppressed dislocation behavior and limited strain hardening, the plastic deformation of nano-sized grains is generally carried by shear band nucleation and propagation. Distinct from the conventional catastrophic shear bands developed in the homogeneous nanostructured material where they only form in the region near fracture and generally only one or several shear bands are developed to accommodate imposed global strain, here dense and dispersed shear bands are formed in our heterogeneous nanostructured sample, as shown in Figs. 4-6. The formation of dispersed shear bands is believed closely related to the microstructural heterogeneity with the NTBs resist shear bands propagations, as frequently seen in the heterostructured materials [47].

The shear banding, as a localized deformation mode, always takes place along the macroscopic planes with largest resolved shear stresses and is dominated by collective shearing of many neighboring grains along their aligned grain boundaries [45,52–55]. Consequently, the shear banding is generally believed to be crystallographic orientation (texture) independent. To verify that the anisotropic behavior is not linked to potential texture developed in the NG matrix, we further measured the inclination angles of shear bands with respect to the tensile axis. For the parallel tension, the average shear band inclination angle is 44.2 ± 6.7°, whereas for the normal tension, it is 46.8 ± 6.4°. Evidently, both values are close to each other and approximately equal to 45°, irrespective of the sample orientation. Therefore, the anisotropic plastic behavior in heterogeneous nanostructured Cu can be believed predominately related to the interactions between shear bands in NG matrix and the anisotropic NTBs.

When the shear bands initiated in NG matrix are stopped by the NTBs, strong stress concentration will be developed at the NTBs/NG interfaces [56]. Owning the strong mechanical anisotropy in nanotwinned structure [32], different reactions will take place in NTBs of different orientations to accommodate the impingement of shear bands. For sample-N, the TBs are normal to the tensile axis, the stress concentration at NTBs/NG interfaces is not high enough to activate the Hard Mode I deformation in nanotwins at the small applied strain (< 1.0%), owing to the strong nanoscale TBs that serves as strong barriers to dislocation glide under this deformation mode and thus nucleate dislocations and make them transmit across the nanoscale TBs requires stresses higher than nucleating shear bands in nanograins [32]. As an evidence, no plastic strain was detected in the NT region (Fig. 3(b1)) until the internal stress caused by the accumulation of shear bands is intensive enough at the higher applied strains of 1.5 ~ 2.0% (after the necking point). Caused by the fact that the shear bands in NG matrix are strongly impeded by the NTBs, significant strain partitioning appeared in the sample-N.

By contrast, when the tensile direction is parallel to TBs, like the case of sample-P, the deformation in NTBs is dominated by Hard Mode II, namely threading dislocations propagating parallel to TBs, which can be activated under a much lower critical stress than the Hard Mode I in sample-N [32]. As a consequence, once a shear band forming in the NG matrix propagates to a nanotwin bundle in the sample-P, the local stress concentration could be sufficiently high to nucleate threading dislocations from the tip of the shear band. This is evidenced by the SEM observations in Fig. 9, the line-like deformation features can already be detected inside the NTBs of sample-P at the applied strain of 1.0%, bearing a strong resemblance to the “zigzag” slip bands in homogeneous nanotwinned Cu under cyclic deformation with the same loading direction [57,58], where the “zigzag” slip bands are attributed to collective motion of threading dislocations linked by common misfit segments on TBs [59]. Caused by such interactions between shear bands and threading dislocation slips in nanotwins, the shear strain can effectively transmit from NG matrix to NTBs. Meanwhile, to sustain the constant external applied strain rates, new shear bands are nucleated repeatedly, which further make the strain uniformly distributed transversely along the interfaces between the NTBs and the NG matrix. As a result, no significant strain incompatibility was built up and thus microscopic strain partitioning did not take place in the sample-P.

The deformation incompatibility in sample-I is created by the NTBs that start yielding first to produce plastic strain, while the NG matrix remains elastic. However, because the NTBs are completely surrounded by the NG matrix, their deformation will be strictly restricted, which results in stress concentrations at the NTBs/NG interfaces and transfers the deformation to the NG matrix. As evidenced by the DIC results in Fig. 3 (c1), a certain average strain of ~0.15% is already detected in NG matrix at the applied strain of 1.0%, where the strain ratio of hard/soft (i.e., $1/R$) is 0.31 (see Table. 1), much higher than the R value of 0.07 in sample-N at the same applied strain, suggesting a reduced strain partitioning in sample-I, compared with that in sample-N.

As concerned by strain gradient plasticity theory [60,61], strain (or stress) gradient at the interface of HARD and SOFT generates

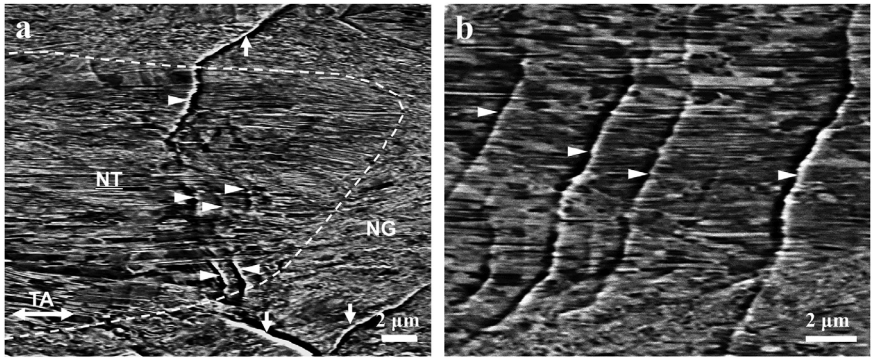

Fig. 9. SEM images showing slip bands crossing NTBs in the sample-P with 1.0% applied strain: (a) the slip bands (indicated by white triangles) in the NTBs connected with the shear bands (indicated by white arrows) in the NG matrix; (b) the magnified view of the slip bands showing a "zigzag" morphology.

geometrically necessary dislocations (GNDs) to accommodate the plastic incompatibility. Importantly, as we presented in this study that the strengthening effect of NTBs can be maximized only when they co-deform with the surrounding NG matrix. Similar conclusion has also been made previously in dual-phase steel [36,46] and lamellar structure [62]. This deformation compatibility is not only related to the strength of individual microstructural component. The ductility as well as the work hardening ability of them under complex stress/strain conditions also play an essential role in mediating the co-deformation of heterogeneous structured materials. Systematic investigations and in-depth quantitative understanding are still highly demanded on the relationship between deformation compatibility and comprehensive mechanical behavior of the heterogeneous structures.

4. Conclusions

Orientation effect of bulk heterogeneous nanostructured Cu composed hybrid structure of isotropic NG matrix and anisotropic NTBs were investigated by tension test with loading directions parallel, normal, and 45° inclined to TBs. We revealed that the strengthening effect of nanotwins in the heterogeneous nanostructure is dominated by both the nanotwins strength and their deformation compatibility with surrounding NG matrix. Only when co-deformation is activated in the two components, the nanotwins could exert substantial strengthening effect (parallel orientation); otherwise, the strengthening effect cannot be fully functional (normal orientation). The orientation-dependent deformation compatibility is owing to the anisotropic deformation behavior of nanotwins and associated interactions with the isotropic shear bands in NG matrix. These results advance our fundamental understanding about the relationship between the deformation compatibility and the mechanical properties in the heterogeneous nanostructures, and insight the design of new heterogeneous structure.

Declaration of Competing Interest

The authors declare that they have no known competing financial interests or personal relationships that could have appeared to influence the work reported in this paper.

Acknowledgments

The authors acknowledge financial support by National Science Foundation of China (NSFC, Grant Numbers. U1608257 and 51931010), the Key Research Program of Frontier Science and International partnership program (Grant Number. GJHZ2029), CAS, and LiaoNing Revitalization Talents Program (Grant Number. XLYC1802026). Z.Y. acknowledges financial support by the National Key R&D Program of China (Grant No. 2017YFA0204403) .

References

[1] L. Lu, Y.F. Shen, X.H. Chen, L.H. Qian, K. Lu, Ultrahigh strength and high electrical conductivity in copper, Science 304 (2004) 422–426.
[2] Y.F. Shen, L. Lu, Q.H. Lu, Z.H. Jin, K. Lu, Tensile properties of copper with nano-scale twins, Scr. Mater. 52 (2005) 989–994.
[3] Z.M. Li, K.G. Pradeep, Y. Deng, D. Raabe, C.C. Tasan, Metastable high-entropy dual-phase alloys overcome the strength–ductility trade-off, Nature 534 (2016) 227–230.
[4] M. Calcagnotto, Y. Adachi, D. Ponge, D. Raabe, Deformation and fracture mechanisms in fine- and ultrafine-grained ferrite/martensite dual-phase steels and the effect of aging, Acta Mater. 59 (2011) 658–670.
[5] X.L. Wu, M.X. Yang, F.P Yuan, G.L Wu, Y.J. Wei, X.X. Huang, Y.T. Zhu, Heterogeneous lamella structure unites ultrafine-grain strength with coarse-grain ductility, Proc. Natl. Acad. Sci. 112 (2015) 14501–14505.
[6] X.L. Wu, Y.T. Zhu, Heterogeneous materials: a new class of materials with unprecedented mechanical properties, Mater. Res. Lett. 5 (2017) 527–532.
[7] Z. Cheng, H.F. Zhou, Q.H. Lu, H.J. Gao, L. Lu, Extra strengthening and work hardening in gradient nanotwinned metals, Science 362 (2018) eaau1925.
[8] K. Lu, Making strong nanomaterials ductile with gradients, Science 345 (2014) 1455–1456.
[9] C. Sawangrat, S. Kato, D. Orlov, K. Ameyama, Harmonic-structured copper: performance and proof of fabrication concept based on severe plastic deformation of powders, J. Mater. Sci. 49 (2014) 6579–6585.
[10] T.H. Fang, W.L. Li, N.R. Tao, K. Lu, Revealing extraordinary intrinsic tensile plasticity in gradient nano-grained copper, Science 331 (2011) 1587–1590.
[11] J.Z. Long, Q.S. Pan, N.R. Tao, M. Dao, S. Suresh, L. Lu, Improved fatigue resistance of gradient nanograined Cu, Acta Mater. 166 (2019) 56–66.
[12] R.Q. Cao, Q. Yu, J. Pan, Y. Lin, A. Sweet, Y. Li, R.O. Ritchie, On the exceptional damage-tolerance of gradient metallic materials, Mater. Today 32 (2019) 94–107.
[13] Y.T. Zhu, X.L. Wu, Perspective on hetero-deformation induced (HDI) hardening and back stress, Mater. Res. Lett. 7 (2019) 393–398.
[14] F.K. Yan, G.Z. Liu, N.R. Tao, K. Lu, Strength and ductility of 316L austenitic stainless steel strengthened by nano-scale twin bundles, Acta Mater. 60 (2012) 1059–1071.
[15] E.W. Qin, L. Lu, N.R. Tao, J. Tan, K. Lu, Enhanced fracture toughness and strength in bulk nanocrystalline Cu with nanoscale twin bundles, Acta Mater. 57 (2009) 6215–6225.
[16] L. Xiong, Z.S. You, S.D. Qu, L. Lu, Fracture behavior of heterogeneous nanostructured 316L austenitic stainless steel with nanotwin bundles, Acta Mater. 150 (2018) 130–138.
[17] L. Xiong, Z.S. You, L. Lu, Enhancing fracture toughness of nanotwinned austenitic steel by thermal annealing, Scr. Mater. 119 (2016) 55–59.
[18] S.S. Luo, Z.S. You, L. Lu, Intrinsic fracture toughness of bulk nanostructured Cu with nanoscale deformation twins, Scr. Mater. 133 (2017) 1–4.
[19] L. Lu, Y.F. Shen, X.H. Chen, L.H. Qian, K. Lu, Ultrahigh strength and high electrical conductivity in copper, Science 304 (2004) 422–426.
[20] K. Lu, L. Lu, S. Suresh, Strengthening materials by engineering coherent internal boundaries at the nanoscale, science 324 (2009) 349–352.
[21] S.W. Kim, X.Y. Li, H.J. Gao, S. Kumar, In situ observations of crack arrest and bridging by nanoscale twins in copper thin films, Acta Mater. 60 (2012) 2959–2972.
[22] Y.S. Li, Y. Zhang, N.R. Tao, K. Lu, Effect of thermal annealing on mechanical properties of a nanostructured copper prepared by means of dynamic plastic deformation, Scr. Mater. 59 (2008) 475–478.
[23] Y. Zhang, N.R. Tao, K. Lu, Mechanical properties and rolling behaviors of nano–grained copper with embedded nano-twin bundles, Acta Mater. 56 (2008) 2429–2440.

[24] F.K. Yan, H.W. Zhang, N.R. Tao, K. Lu, Quantifying the microstructures of pure Cu subjected to dynamic plastic deformation at cryogenic temperature, J. Mater. Sci. Technol. 27 (2011) 673–679.
[25] G.H. Xiao, N.R. Tao, K. Lu, Microstructures and mechanical properties of a Cu–Zn alloy subjected to cryogenic dynamic plastic deformation, Mater. Sci. Eng. A 513-514 (2009) 13–21.
[26] G.H. Xiao, N.R. Tao, K. Lu, Strength–ductility combination of nanostructured Cu–Zn alloy with nanotwin bundles, Scr. Mater. 65 (2011) 119–122.
[27] Y. Zhang, N.R. Tao, K. Lu, Effects of stacking fault energy, strain rate and temperature on microstructure and strength of nanostructured Cu–Al alloys subjected to plastic deformation, Acta Mater. 59 (2011) 6048–6058.
[28] H.T. Wang, N.R. Tao, K. Lu, Strengthening an austenitic Fe–Mn steel using nanotwinned austenitic grains, Acta Mater. 60 (2012) 4027–4040.
[29] B.B. Zhang, F.K. Yan, M.J. Zhao, N.R. Tao, K. Lu, Combined strengthening from nanotwins and nanoprecipitates in an iron-based superalloy, Acta Mater. 151 (2018) 310–320.
[30] L.X. Sun, N.R. Tao, K. Lu, A high strength and high electrical conductivity bulk CuCrZr alloy with nanotwins, Scr. Mater. 99 (2015) 73–76.
[31] F.K. Yan, Q. Li, N.R. Tao, Anisotropic strengthening of nanotwinned austenitic grains in a nanotwinned stainless steel, Scr. Mater. 142 (2018) 15–19.
[32] Z.S. You, X.Y. Li, L.J. Gui, Q.H. Lu, T. Zhu, H.J. Gao, L. Lu, Plastic anisotropy and associated deformation mechanisms in nanotwinned metals, Acta Mater. 61 (2013) 217–227.
[33] T. Zhu, H.J. Gao, Plastic deformation mechanism in nanotwinned metals: an insight from molecular dynamics and mechanistic modeling, Scr. Mater. 66 (2012) 843–848.
[34] M. Huang, C. Xu, G.H. Fan, E. Maawad, W.M Gan, L. Geng, F.X. Lin, G.Z. Tang, H. Wu, Y. Du, D.Y. Li, K.S. Miao, T.T. Zhang, X.S. Yang, Y.P. Xia, G.J. Cao, H.J. Kang, T.M. Wang, T.Q. Xiao, H.L. Xie, Role of layered structure in ductility improvement of layered Ti-Al metal composite, Acta Mater. 153 (2018) 235–249.
[35] J. Kadkhodapour, A. Butz, S. Ziaei-Rad, S. Schmauder, A micro mechanical study on failure initiation of dual phase steels under tension using single crystal plasticity model, Int. J. Plast. 27 (2011) 1103–1125.
[36] K. Park, M. Nishiyama, N. Nakada, T. Tsuchiyama, S. Takaki, Effect of the martensite distribution on the strain hardening and ductile fracture behaviors in dual-phase steel, Mater. Sci. Eng. A 604 (2014) 135–141.
[37] J.Y. He, F.P. Yuan, M.X. Yang, S.H. Jiao, X.L. Wu, Superior mechanical properties and deformation mechanisms of heterogeneous laminates under dynamic shear loading, Mater. Sci. Eng. A 756 (2019) 492–501.
[38] E. Ma, T. Zhu, Towards strength–ductility synergy through the design of heterogeneous nanostructures in metals, Mater. Today 20 (2017) 323–331.
[39] F.K. Yan, N.R. Tao, F. Archie, I. Gutierrez-Urrutia, D. Raabe, K. Lu, Deformation mechanisms in an austenitic single-phase duplex microstructured steel with nanotwinned grains, Acta Mater. 81 (2014) 487–500.
[40] F.K. Yan, N.R. Tao, K. Lu, Tensile ductility of nanotwinned austenitic grains in an austenitic steel, Scr. Mater. 84-85 (2014) 31–34.
[41] Q. Li, F.K. Yan, N.R. Tao, Enhanced fatigue damage resistance of nanotwinned austenitic grains in a nanotwinned stainless steel, Scr. Mater. 136 (2017) 59–63.
[42] Q. Li, F.K. Yan, N.R. Tao, D. Ponge, D. Raabe, K. Lu, Deformation compatibility between nanotwinned and recrystallized grains enhances resistance to interface cracking in cyclic loaded stainless steel, Acta Mater. 165 (2019) 87–98.
[43] Y.S. Li, N.R. Tao, K. Lu, Microstructural evolution and nanostructure formation in copper during dynamic plastic deformation at cryogenic temperatures, Acta Mater. 56 (2008) 230–241.
[44] N.R. Tao, K. Lu, Dynamic plastic deformation (DPD): a novel technique for synthesizing bulk nanostructured metals, J. Mater. Sci. Technol. 23 (2007) 771–774.
[45] M.A. Meyers, A. Mishra, D.J. Benson, Mechanical properties of nanocrystalline materials, Prog. Mater. Sci. 51 (2006) 427–556.
[46] Y. Tomota, I. Tamura, Mechanical behavior of steels consisting of two ductile phases, Trans. Iron Steel Inst. Jpn. 22 (1982) 665–677.
[47] Y.F. Wang, C.X. Huang, Q. He, F.J. Guo, M.S. Wang, L.Y. Song, Y.T. Zhu, Heterostructure induced dispersive shear bands in heterostructured Cu, Scr. Mater. 170 (2019) 76–80.
[48] R. Pippan, A. Hohenwarter, The importance of fracture toughness in ultrafine and nanocrystalline bulk materials, Mater. Res. Lett. 4 (2016) 127–136.
[49] A. Hohenwarter, R. Pippan, Fracture and fracture toughness of nanopolycrystalline metals produced by severe plastic deformation, Philos. Trans. R. Soc., A 373 (2015) 20140366.
[50] A. Hohenwarter, R. Pippan, Anisotropic fracture behavior of ultrafine-grained iron, Mater. Sci. Eng. A 527 (2010) 2649–2656.
[51] A. Hohenwarter, R. Pippan, Fracture toughness evaluation of ultrafine-grained nickel, Scr. Mater. 64 (2011) 982–985.
[52] S. Cheng, E. Ma, Y.M. Wang, L.J. Kecskes, K.M. Youssef, C.C. Koch, U.P. Trociewitz, K. Han, Tensile properties of in situ consolidated nanocrystalline Cu, Acta Mater. 53 (2005) 1521–1533.
[53] J.E. Carsley, A. Fisher, W.W. Milligan, E.C. Aifantis, Mechanical behavior of a bulk nanostructured iron alloy, Metall. Mater. Trans. A 29 (1998) 2261–2271.
[54] K. Yang, Y. Ivanisenko, A. Caron, A. Chuvilin, L. Kurmanaeva, T. Scherer, R.Z. Valiev, H.J. Fecht, Mechanical behaviour and in situ observation of shear bands in ultrafine grained Pd and Pd–Ag alloys, Acta Mater 58 (2010) 967–978.
[55] H. Guo, E. Jürgen, L.S. Wolfgang, S. Ludwig, Novel Ti-base nanostructure-dendrite composite with enhanced plasticity, Nat. Mater. 2 (2003) 33–37.
[56] N. Jia, F. Roters, P. Eisenlohr, D. Raabe, X. Zhao, Simulation of shear banding in heterophase co-deformation: example of plane strain compressed Cu–Ag and Cu–Nb metal matrix composites, Acta Mater. 61 (2013) 4591–4606.
[57] Q.S. Pan, Q.H. Lu, L. Lu, Fatigue behavior of columnar-grained Cu with preferentially oriented nanoscale twins, Acta Mater. 61 (2013) 1383–1393.
[58] Q.S. Pan, L. Lu, Strain-controlled cyclic stability and properties of Cu with highly oriented nanoscale twins, Acta Mater. 81 (2014) 248–257.
[59] Q.S. Pan, H.F. Zhou, Q.H. Lu, H.J. Gao, L. Lu, History-independent cyclic response of nanotwinned metals, Nature 551 (2017) 214–217.
[60] H.J. Gao, Y.G. Huang, Geometrically necessary dislocation and size-dependent plasticity, Scr. Mater. 48 (2003) 113–118.
[61] M.F. Ashby, The deformation of plastically non-homogeneous materials, Philos. Mag. 21 (1970) 399–424.
[62] B. Gao, Q.Q. Lai, Y. Cao, R. Hu, L.R. Xiao, Z.Y. Pan, N.N. Liang, Y.S. Li, G. Sha, M.P. Liu, H. Zhou, X.L. Wu, Y.T. Zhu, Ultrastrong low-carbon nanosteel produced by heterostructure and interstitial mediated warm rolling, Sci. Adv. 6 (2020) eaba8169.